Frontiers of Information Technology & Electronic Engineering
www.jzus.zju.edu.cn; engineering.cae.cn; www.springerlink.com
ISSN 2095-9184 (print); ISSN 2095-9230 (online)
E-mail: jzus@zju.edu.cn

Enhanced collection of scattered photons in nonlinear fluorescence microscopy by extended epi-detection with a silicon photomultiplier array*

Ruheng SHI[1], Cheng JIN[1], Chi LIU[1], Lingjie KONG[†‡1,2]

[1]*State Key Laboratory of Precision Measurement Technology and Instruments, Department of Precision Instrument, Tsinghua University, Beijing 100084, China*

[2]*IDG/McGovern Institute for Brain Research, Tsinghua University, Beijing 100084, China*

[†]E-mail: konglj@tsinghua.edu.cn

Received Aug. 12, 2020; Revision accepted Nov. 6, 2020; Crosschecked Dec. 24, 2020; Published online Jan. 29, 2021

Abstract: To maximize signal collection in nonlinear optical microscopy, non-descanned epi-detection is generally adopted for in vivo imaging. However, because of severe scattering in biological samples, most of the emitted fluorescence photons go beyond the collection angles of objectives and thus cannot be detected. Here, we propose an extended detection scheme to enhance the collection of scattered photons in nonlinear fluorescence microscopy using a silicon photomultiplier array ahead of the front apertures of objectives. We perform numerical simulations to demonstrate the enhanced fluorescence collection via extended epi-detection in the multi-photon fluorescence imaging of human skin and mouse brain through craniotomy windows and intact skulls. For example, with red fluorescence emission at a depth of 600 μm in human skin, the increased collection can be as much as about 150% with a 10×, 0.6-NA objective. We show that extended epi-detection is a generally applicable, feasible technique for use in nonlinear fluorescence microscopy to enhance signal detection.

Key words: Extended epi-detection; Enhanced collection; Nonlinear fluorescence microscopy; Silicon photomultiplier array
https://doi.org/10.1631/FITEE.2000410 **CLC number:** O439

1 Introduction

Fluorescence microscopy has found its niche in biomedical studies due to its non-invasive and specific capability in the observation of biodynamics (Lichtman and Conchello, 2005). However, biological samples are turbid by nature, with optical properties characterized by scattering, absorption, and anisotropy factor *g* (Cheong et al., 1990; Jacques, 2013). In one-photon fluorescence imaging, both excitation and emission lights suffer from strong scattering and blood absorption at visible wavelengths (Oheim et al., 2001; Wang MR et al., 2019). The scattering reduces the penetration depth of the excitation light and introduces cross-talk in the emission light, which further reduces the imaging depth. To alleviate scattering, laser-scanning multiphoton microscopy (MPM) has been proposed, in which longer excitation wavelengths are used (Denk et al., 1990). Moreover, benefiting from nonlinear effects, the nonlinear excitation is localized in MPM, which ensures that all the emitted photons including ballistic and scattered photons contribute as useful signals (Denk et al., 1990; Jin et al., 2020). Thus, for the maximal signal collection, non-descanned epi-detection is generally

‡ Corresponding author

* Project supported by the National Natural Science Foundation of China (Nos. 61831014 and 61771287), the Tsinghua University Initiative Scientific Research Program, China (No. 20193080076), and the Graduate Education Innovation Grants, Tsinghua University, China (No. 201905J003)

ORCID: Ruheng SHI, https://orcid.org/0000-0001-7993-708X; Lingjie KONG, https://orcid.org/0000-0002-8250-7547

adopted for in vivo multiphoton imaging, with single-element detectors such as photomultiplier tubes (PMTs) placed close to the back pupil of excitation objectives (Denk et al., 1990). Unfortunately, due to the limited collection capability of objectives, severe scattering leads to the miss-detection of most fluorescence photons; i.e., the current detection schemes have low collection efficiency. Several strategies have been proposed to collect missed photons that cannot pass through the objectives. Combs et al. (2007) used a parabolic mirror to reflect missed photons to the detector. Dvornikov and Gratton (2016) adopted a wide-area PMT to collect the transmitted fluorescence signals. However, these methods are used for collecting transmitted signals, and thus are not suitable for in vivo imaging of thick, non-transparent samples. Engelbrecht et al. (2009) collected additional fluorescence photons using a ring of optical fibers surrounding the front aperture of the objectives, but in this method the fiber coupling efficiency could be a problem. Extended detection has been demonstrated to enhance the collection of back-scattered pump/probe signals in stimulated Raman imaging, where a large-area silicon PiN photodiode with a hole in the center is placed before the front aperture of the objectives. This scheme enables the first video-rate molecule imaging in vivo (Saar et al., 2010) and the rapid detection of brain tumors (Ji et al., 2013).

However, the extended detection of back-scattered fluorescence signals has not been demonstrated in nonlinear fluorescence microscopy, in which wide-area, bulky, and expensive PMTs (Denk et al., 1990) or hybrid photodetectors (Chen et al., 2016) are required. Recently, silicon photomultipliers (SiPMs) with a large active area have been developed, with advantages of low cost and low pulse height variability. Placed close to the back pupil of excitation objectives, SiPMs have been used in two-photon imaging of neural activity (Modi et al., 2019) and coherent anti-Stokes Raman scattering imaging of oil (Allen et al., 2020). SiPMs have been shown to match the signal-to-noise ratio of PMTs at photon rates encountered in calcium imaging and outperform PMTs at high photon rates, i.e., in high-photon-rate voltage imaging (Modi et al., 2019).

In this study, we investigate the feasibility and robustness of extended epi-detection in nonlinear fluorescence microscopy via numerical simulations. A large-area detector is modeled by mosaicking commercial SiPMs (S13360-6075PE, Hamamatsu), with dimensions of 6 mm×6 mm×1.45 mm and quantum efficiency of about 48% at 525 nm (close to, or higher than the quantum efficiency of the selected GaAsP PMTs). We investigate the enhanced collection efficiency of extended epi-detection in the multiphoton fluorescence imaging of a human skin model, a mouse brain model, and a hybrid model of skull-brain, with different fluorescent proteins.

2 Extended epi-detection scheme and simulation model

In Figs. 1a and 1b, we show the scheme of extended epi-detection, in which we attach an SiPM array ahead of the front aperture of the objective. To block the back-scattered excitation light, a filter is placed between the sample and the SiPM array. In this setup, back-scattered fluorescence signals can be collected by the excitation objective and SiPM array, which has a hole drilled in the center.

We used the Henyey-Greenstein distribution (Toublanc, 1996) to model the bio-sample scattering, Zemax (OpticStudio) to simulate the photon propagation, and custom MATLAB scripts for statistical analysis. To simulate the incoherent emission of fluorescence in multiphoton fluorescence microscopy, we first generated a large number of rays (10^5) from a point in the simulated bio-samples, and then calculated the spatial distribution of emitted light in the plane of the SiPM surface. Specifically, the collection numerical aperture (NA) of the objective was simulated by limiting the acceptance angle.

In the extended detection scheme, a hole is drilled in the center of the SiPM array, whose size is critical for the collection of scattered photons. As shown in Fig. 1b, the hole radius (r) is determined by the thicknesses of the filter (d_f) and SiPM (d_s), the penetration depth (d_p), the one-half angular aperture of the objective (θ), and the effective field-of-view (FOV). Specifically, there is a trade-off between the effective FOV and signal enhancement benefiting from extended detection; i.e., drilling smaller holes ensures higher signal collection efficiency, but lowers the effective FOV. To make a compromise, we set the effective FOV as 1/3 of the maximal FOV supported

by the objectives. Based on the practical needs of bio-imaging in a large FOV and at a high resolution, we chose a low magnification, high NA objective (10×, 0.6-NA, XLPLN10XSVMP, Olympus) for the simulations, unless specified. Accordingly, we set the radii of the drilled holes based on the maximum imaging depths in different models with θ about 26°48′, effective FOV about 600 μm, d_f about 0.5 mm, and d_s about 1.45 mm. The immersion medium was water. We set the size of the SiPM array (with radius R) according to the practical sizes of the optical windows.

As an example, we simulated photon propagation at a depth of 200 μm in human skin (refraction index=1.41) (Lister et al., 2012). Figs. 1a and 1e show the walk trajectory of the emitted fluorescence (emission wavelength=630 nm) inside the bio-sample and the distribution of scattering clouds at the detector surface (radius=12 mm), respectively. In Fig. 1a, the emission photons are classified into three types: the back-scattered fluorescence (in green) that can be collected by extended epi-detection, the transmitted fluorescence (in blue) that can pass through the bio-sample, and the absorbed fluorescence (in red) that can be absorbed. As shown in Fig. 1e, only about 13.44% of the fluorescence photons fall in the acceptance angle of the objective, even though about 19.77% of the fluorescence photons fall in the front aperture of the objective. However, an additional about 13.23% of the fluorescence photons can be detected by the SiPM; i.e., about 26.67% of the fluorescence photons in total can be collected in the combined collection mode (including photons collected by the objective and SiPM).

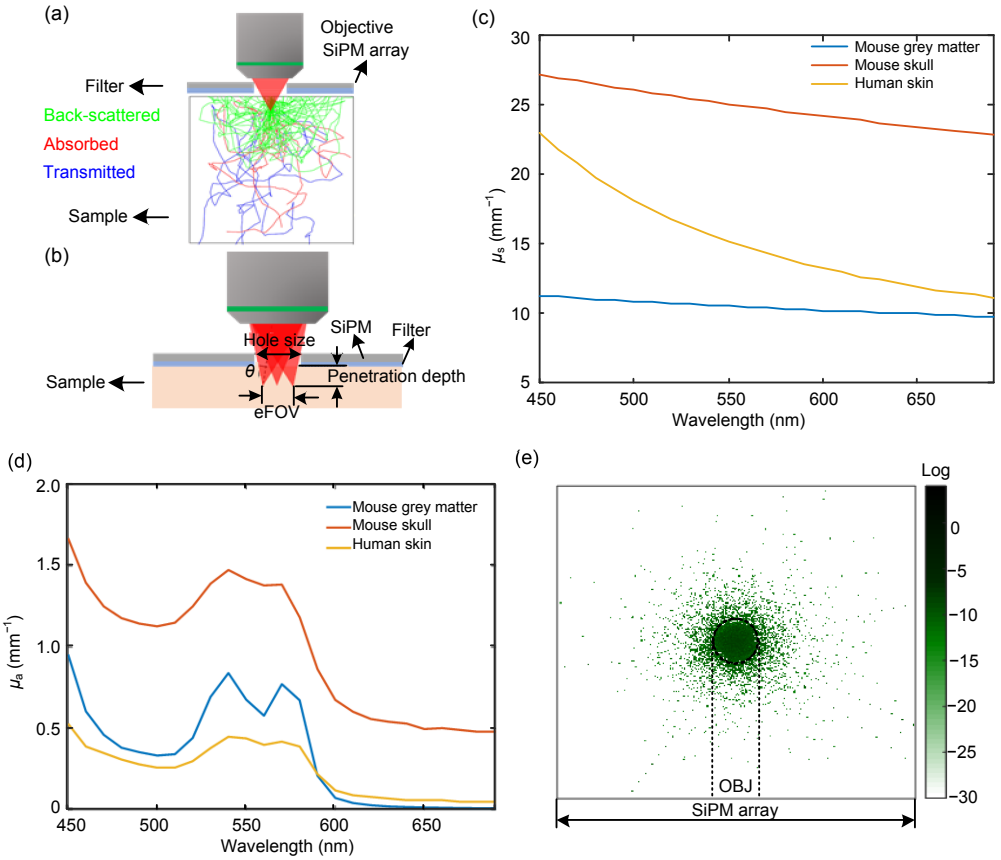

Fig. 1 Extended epi-detection model, tissue optical properties, and an example of fluorescence photon distribution

(a) Extended epi-detection scheme; (b) An add-on strategy of an extended detector (θ is the one-half angular aperture of the objective, and eFOV indicates the effective field-of-view); (c) Scattering coefficient μ_s for human skin, mouse brain grey matter, and mouse skull; (d) Absorption coefficient μ_a for human skin, mouse brain grey matter, and mouse skull; (e) An example of fluorescence photon (emission wavelength=630 nm) distribution at the SiPM surface, emitting from a depth of 200 μm in human skin (the black dotted circle shows the collection area of the objective). References to color refer to the online version of this figure

3 Simulation results of enhanced collection via extended epi-detection

3.1 Extended epi-detection in the human skin model

We quantitatively analyzed the effect of extended epi-detection in the imaging of human skin. The factor g was set as 0.8 (Cheong et al., 1990; Jacques, 2013), and the size of the human skin model was set as 2.4 cm×2.4 cm×4 mm. The radius of the SiPM array was set as R=6 mm. We set the radius of the hole as 1.55 mm for an imaging depth of <600 μm and effective FOV=600 μm. Fig. 2a shows the collection efficiency of auto-fluorescence at 525 nm (abbreviated as GAF). The extended epi-detection boosts the collection efficiency at each imaging depth within the whole effective FOV. In particular, for fluorescence sources either in the center or at the edge of the effective FOV, the collection efficiency of the objective remains nearly constant. In comparison, using SiPM, the collection efficiency of fluorescence sources at the edge of the effective FOV would be higher as scattered photons are more likely to hit the extended detector. Thus, the combined collection efficiency for fluorescence sources at the edge of the effective FOV will be higher, as expected. For example, at an imaging depth of 600 μm, the collection efficiency (expressed as mean±SD with n=5) varies from (4.73±0.01)% in the objective collection mode to (6.83±0.12)% in the combined collection mode for GAF sources in the center of the FOV (magenta curve in Fig. 2a) and from (4.46±0.03)% (objective

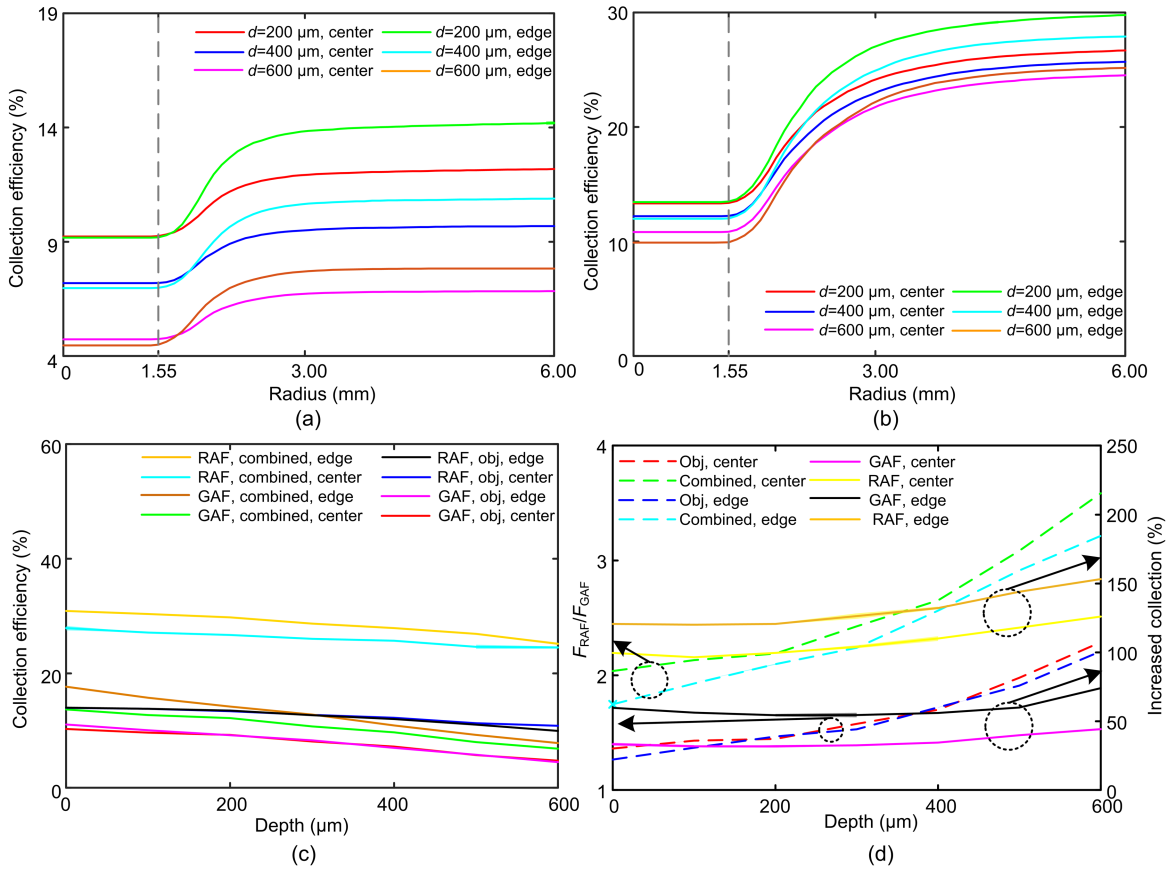

Fig. 2 Enhanced collection via extended epi-detection in the human skin model

Collection efficiency versus detection radius at different imaging depths for GAF (a) and RAF (b) (The dotted gray lines show the radius of the drilled hole in the center of the extended detector, "center" and "edge" refer to the fluorescent sources in the center and at the edge of the FOV respectively, and d represents the imaging depth); (c) Collection efficiency versus imaging depth in the objective collection mode and combined collection mode; (d) Collection efficiency ratio of the RAF and GAF at different imaging depths in the objective collection mode and combined collection mode (left vertical axis), and the increased collection of GAF and RAF as a function of the imaging depth (right vertical axis) (The dotted lines correspond to the left vertical axis, and the solid lines correspond to the right vertical axis). References to color refer to the online version of this figure

collection only) to (7.83±0.08)% (combined collection) for GAF sources at the edge of the FOV (deep yellow curve in Fig. 2a).

The same trends can be seen for autofluorescence emission at 630 nm (abbreviated as RAF) in Fig. 2b. For example, at a depth of 200 μm, the collection efficiency of RAF varies from (13.44±0.02)% (objective collection only) to (26.67±0.06)% (combined collection) for fluorescence sources in the center of the FOV (red curve in Fig. 2b) and from (13.34±0.04)% (objective collection only) to (29.76±0.11)% (combined collection) for fluorescence sources at the edge of the FOV (green curve in Fig. 2b). Comparing Figs. 2a and 2b, we know that at the same imaging depth and with the same extended detection radius, the collection efficiency of RAF is higher than that of GAF due to the smaller scattering and absorption coefficients of RAF.

Fig. 2c shows the collection efficiency versus imaging depth. As discussed above, in the objective collection mode, the collection efficiency remains nearly constant across the FOV for GAF (magenta and red lines in Fig. 2c) and RAF (black and blue lines in Fig. 2c). In the combined collection mode, the collection efficiency in the edge of the FOV is higher than that at the center of the FOV, for GAF (deep yellow and green lines in Fig. 2c) and RAF (light yellow and cyan lines in Fig. 2c). The collection efficiency drops when the imaging depth increases due to the scattering and absorption. For example, the collection efficiency of RAF signals at the edge of the FOV (the light yellow line) varies from (30.9±0.1)% (d=0 μm) to (25.17±0.21)% (d=600 μm) in the combined collection mode.

Fig. 2d shows the ratio of the collection efficiency of RAF fluorescence and GAF fluorescence ($F_{\mathrm{RAF}}/F_{\mathrm{GAF}}$, left vertical axis) and the increased collection (right vertical axis) induced by extended epi-detection as a function of the imaging depth. We define the increased collection as

$$\text{Increased collection}=\frac{\mathrm{CE}_{\mathrm{combined}}-\mathrm{CE}_{\mathrm{obj}}}{\mathrm{CE}_{\mathrm{obj}}}\times 100\%, \quad (1)$$

where $\mathrm{CE}_{\mathrm{combined}}$ indicates the collection efficiency in the combined collection mode and $\mathrm{CE}_{\mathrm{obj}}$ represents the collection efficiency in the objective collection mode. When the imaging depth is increased, the benefit of using fluorophores of a larger emission wavelength becomes more apparent. For example, $F_{\mathrm{RAF}}/F_{\mathrm{GAF}}$ is 1.748±0.010 at a depth of 0 μm and 3.215±0.090 at a depth of 600 μm for fluorescent sources at the edge of the FOV in the combined collection mode. The increased collection efficiencies for RAF and GAF persist at increased imaging depths, which is beneficial for deep tissue imaging. For example, the increased collection efficiency of RAF fluorescence is (153.2±1.8)% (d=600 μm) for fluorescent sources at the edge of the FOV.

3.2 Extended epi-detection in the mouse brain model

We examined whether such an extended detection scheme is effective in a mouse brain model. The factor g was set as 0.9 (Cheong et al., 1990; Jacques, 2013). The size of the mouse brain model was set as 1.3 cm×1 cm×6.5 mm, and the refraction index of the mouse brain grey matter was 1.37 (Binding et al., 2011). To collect as many fluorescence photons as possible, we set a large cranial window with 5-mm diameter (i.e., R=2.5 mm) covered with a 170-μm-thick coverslip (Holtmaat et al., 2009). We set the radius of the central hole in the SiPM as 1.83 mm for an imaging depth of <1.2 mm.

Figs. 3a and 3b show the collection efficiencies of green fluorescence protein (GFP, emission wavelength=525 nm) and red fluorescence protein (RFP, emission wavelength=630 nm) versus the extended detection radius, respectively. As expected, extended detection also boosts collection efficiency in the mouse brain model. For example, at an imaging depth of 200 μm, the collection efficiency of GFP varies from (5.90±0.01)% (objective collection only) to (9.30±0.05)% (combined collection) for fluorescence sources in the center of the FOV and from (6.04±0.02)% (objective collection only) to (10.16±0.12)% (combined collection) for fluorescence sources at the edge of the FOV; the collection efficiency of RFP varies from (11.02±0.06)% (objective collection only) to (20.47±0.11)% (combined collection) for fluorescence sources at the center of the FOV and from (10.95±0.05)% (objective collection only) to (22.31±0.11)% (combined collection) for fluorescence sources at the edge of the FOV. Further analysis is shown in Figs. 3c and 3d. Fig. 3c shows the collection efficiency versus imaging depth in the objective

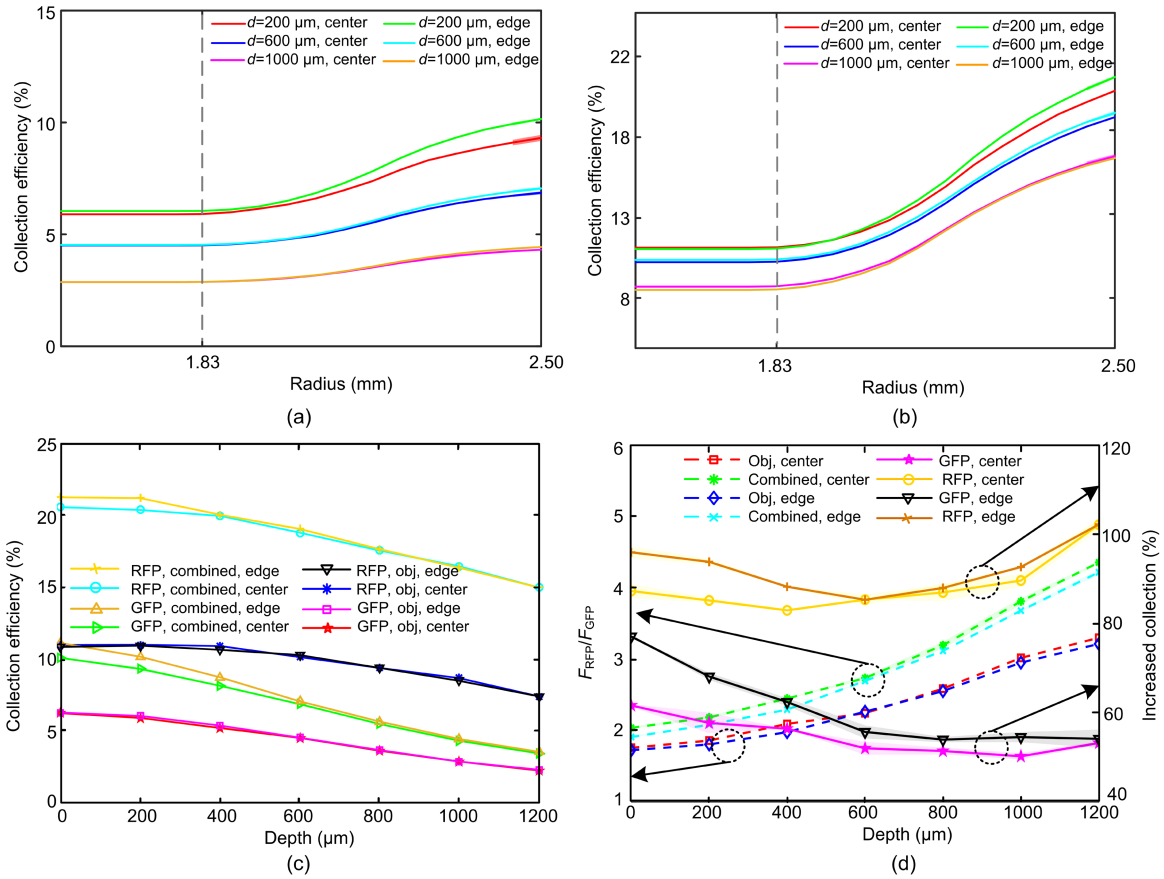

Fig. 3 Enhanced collection via extended epi-detection in the mouse brain model

Collection efficiency versus detection radius at different imaging depths for GFP (a) and RFP (b) (The dotted gray lines show the radius of the drilled hole in the center of the extended detector, "center" and "edge" refer to fluorescent sources in the center and at the edge of the FOV respectively, and *d* represents the imaging depth); (c) Collection efficiency versus imaging depth in the objective collection mode and combined collection mode; (d) Collection efficiency ratio of the RFP and GFP at different imaging depths in the objective collection mode and combined collection mode (left vertical axis), and the increased collection of GFP and RFP as a function of the imaging depth (right vertical axis) (The dotted lines correspond to the left vertical axis and the solid lines correspond to the right vertical axis). References to color refer to the online version of this figure

collection mode and combined collection mode. The collection efficiency drops when the imaging depth increases. Also, the collection efficiency curves for fluorescent sources in the center and at the edge of the FOV almost overlap, which suggests that the position dependence of fluorescence sources is minor here due to the limited extended detector size in the mouse brain model. Fig. 3d shows the ratio of the RFP fluorescence and GFP fluorescence (F_{RFP}/F_{GFP}, left vertical axis) and the increased collection (right vertical axis) induced by extended epi-detection as a function of the imaging depth. Similarly, F_{RFP}/F_{GFP} increases for deep imaging. For example, F_{RFP}/F_{GFP} varies from about 2.041 (d=0 μm) to about 4.359 (d=1200 μm) for fluorescent sources in the center of the FOV in the combined collection mode.

We also compared the performance of our scheme with that of the supplementary fiber-optic light collection method (Engelbrecht et al., 2009), with the same simulation parameters. For mouse brain imaging at 800-μm depth labeled with GFP, our method increased the collection by about 51.4%, compared to about 40% using the supplementary fiber-optic light collection method (Engelbrecht et al., 2009).

3.3 Extended epi-detection in the hybrid model of mouse skull and brain

To avoid artifacts arising from immune responses after craniotomy, it is highly desirable to adopt advanced methods for imaging directly through intact skulls (Yang et al., 2010). We have

demonstrated that with two-photon microscopy based on the iterative multi-photon adaptive compensation technique, structures and functional dynamics of dendrites under an intact mouse skull can be monitored (Kong and Cui 2014, 2015a, 2015b). It has also been shown that three-photon microscopy is capable of imaging through intact skulls (Wang TY et al., 2018). In the literature, the scattering of excitation light through skull has been managed while the collection of scattered emission light is untreated. As scattering affects signal collection efficiency, we examined the performance enhancement of extended epi-detection in a hybrid model of mouse skull and brain (Fig. 4a).

Here, we set the thickness of the skull as about 100 μm (Wang TY et al., 2018) with a refraction index of 1.5 (Soleimanzad et al., 2017). The factor g of the skull was set as 0.9 (Cheong et al., 1990; Jacques, 2013). The radius of the central hole in the SiPM (R=2.5 mm) was set as 1.27 mm for an imaging depth of <400 μm under the dura (i.e., the thickness of the skull was not included). Figs. 4b and 4c show the collection efficiencies of the GFP fluorescence and RFP fluorescence versus the detection radius in the hybrid model, respectively. The skull can be considered an additional scatterer (Fig. 1c) and absorber (Fig. 1d). The additional absorption will lower the collection efficiency, and additional scattering will further randomize the walk trajectory of emitted fluorescence. Figs. 4b and 4c show that the extended detection is effective in the presence of the skull. For example, in Fig. 4c, at a depth of 400 μm, the collection efficiency of RFP varies from (10.50±0.05)% to (18.05±0.06)% for fluorescent sources in the center of the FOV (magenta curve) and from (10.70±0.02)% to (18.30±0.03)% for fluorescent sources at the edge of the FOV (deep yellow curve). Fig. 4d shows the collection efficiency at different imaging depths in the objective collection mode and combined collection mode. Due to the limited size of the extended detectors in the hybrid skull-brain model, the position dependence of the fluorescence source is minor here, as suggested by the overlapping of collection efficiency curves for fluorescent sources in the center and at the edge of the FOV. Fig. 4e shows the ratio of the RFP fluorescence and GFP fluorescence (F_{RFP}/F_{GFP}) as a function of the imaging depth. Consistently, as the imaging depth increases, F_{RFP}/F_{GFP} increases. Specifically, F_{RFP}/F_{GFP} changes from about 2.525 (d=0 μm) to about 2.930 (d=400 μm) for fluorescent sources in the center of the FOV in the combined collection mode. Fig. 4f shows the increased collection induced by our proposed scheme as a function of the imaging depth. The increased collection is nearly constant within a superficial depth of 400 μm. For example, for fluorescent sources in the center of the FOV, the increased collection varies from (63.67±0.30)% (d=0 μm) to (71.12±0.49)% (d=400 μm) for RFP and from (26.25±0.67)% (d=0 μm) to (27.09±0.94)% (d=400 μm) for GFP. The enhanced performance in fluorescence collection will improve the signal-to-noise ratio in practical imaging, and thus alleviate the critical requirement for high-energy ultrashort lasers (Wang TY et al., 2018).

4 Discussion and conclusions

In this paper, we report the results of a numerical study of the enhanced collection of emitted fluorescence via an extended epi-detection scheme. Through simulations of a human skin model, a mouse brain model, and a hybrid model of mouse skull and brain, we have shown that such an extended epi-detection scheme is effective in deep tissue imaging. Choosing fluorescence proteins of larger emission wavelength is also beneficial. For example, in the human skin model, the increased collection efficiency of RAF signals was (153.2±1.8)% (d=600 μm) for fluorescent sources at the edge of the FOV. For deep brain imaging, the proposed scheme can improve the fluorescence collection, even in the presence of intact mouse skull.

We have performed the simulations above based on a 10×, 0.6-NA objective. In practice, different objectives are used according to specific imaging needs. We have compared the performance enhancements based on different objectives using the human skin model as an example. We have chosen a pair of objectives with the same magnification but different NAs (10×, 0.6-NA, XLPLN10XSVMP, Olympus, and 10×, 0.5-NA, CFI Plan Apo 10XC Glyc, Nikon), and a pair of objectives with the same NA but different magnifications (16×, 0.8-NA, CFI75 LWD 16X W, Nikon, and 40×, 0.8-NA, LUMPLFLN40XW, Olympus). The diameter of the effective

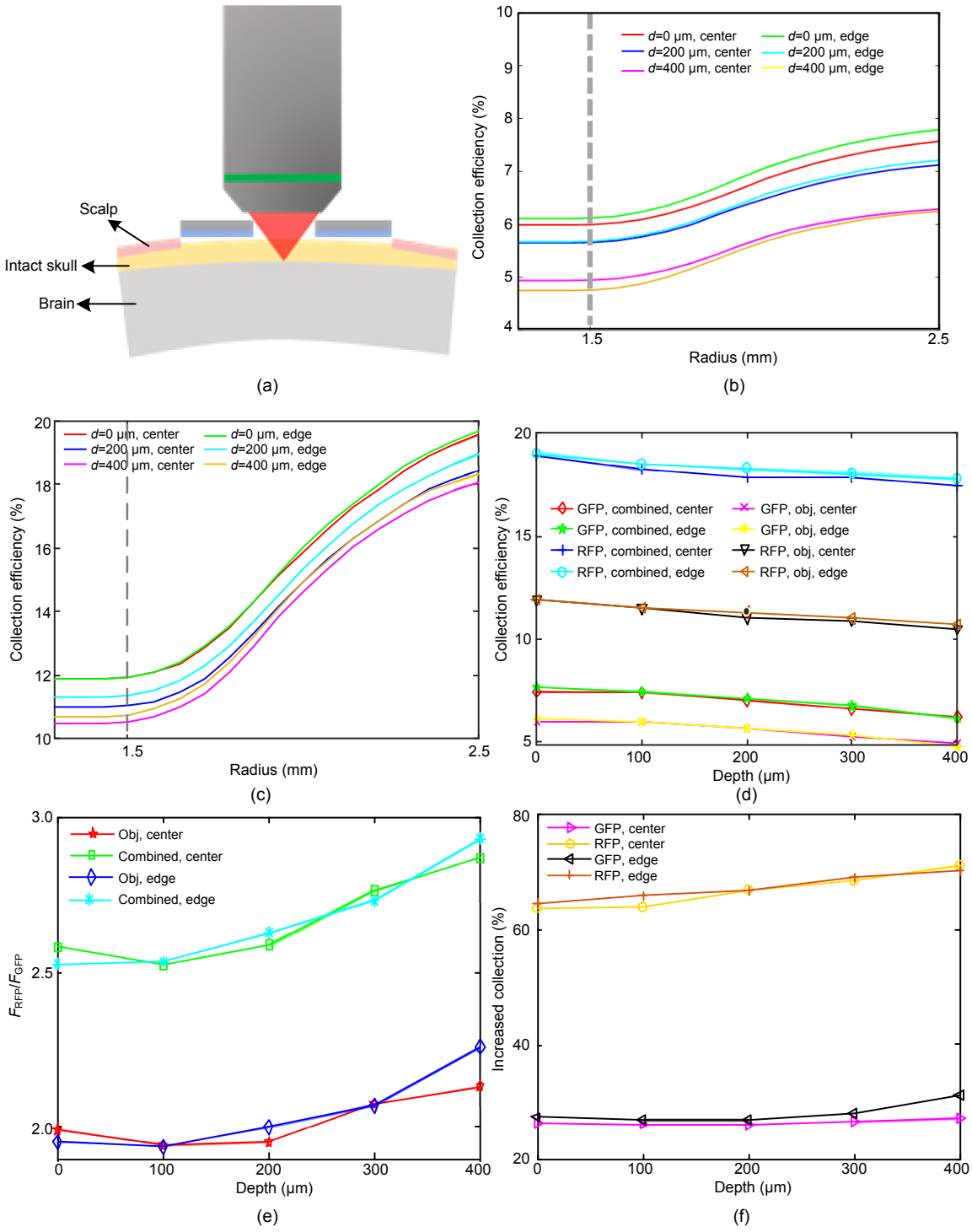

Fig. 4 Enhanced collection via extended epi-detection in a hybrid model of mouse skull and brain

(a) A hybrid model of mouse skull and brain; Collection efficiency versus detection radius at different imaging depths (excluding the thickness of the mouse skull) for GFP (b) and RFP (c) (The dotted gray lines show the radius of the drilled hole in the center of the extended detector, "center" and "edge" refer to the fluorescent sources in the center and at the edge of the FOV respectively, and *d* represents the imaging depth); (d) Collection efficiency at different imaging depths in the objective collection mode and combined collection mode; (e) Collection efficiency ratio of the RFP and GFP at different imaging depths in the objective collection mode and combined collection mode; (f) Increased collection of GFP and RFP as a function of the imaging depth. References to color refer to the online version of this figure

FOV for each objective was set as 600, 600, 400, and 200 μm, corresponding to the radius of the drilled hole in the SiPM as 1.28, 1.55, 2.08 and 1.95 mm, respectively. Figs. 5a and 5b show the increased collection with different objectives for fluorescent sources in the center and at the edge of the FOV, respectively. For objectives of the same magnification (same effective FOV), the enhanced performance is poorer for those with a higher NA, in which the large size of the drilled hole (red and yellow lines in Fig. 5) lowers the collection efficiency. For objectives of the same NA, the enhanced performance is poorer for those with a lower magnification but a larger effective FOV (green and blue lines in Fig. 5). This is consistent with the expected trade-off between effective FOV and signal enhancement resulting from extended detection.

Although in another report (Engelbrecht et al., 2009), the enhanced collection efficiency varied a little for fluorescent sources across the FOV, our proposed scheme can still be used practically for quantitative imaging after calibration. Moreover, in the simulations, we have supposed that the tissue surface was flat across the size of the extended detector, which fits for most bio-samples. For small organs, a curved surface may lower the collection efficiency. In this case, however, an extended detector of a smaller size would still be effective.

In summary, we have demonstrated that extended epi-detection of back-scattered photons is a generally applicable technique in nonlinear fluorescence microscopy to enhance detection signals. Future work could involve implementing the proposed method in practical imaging.

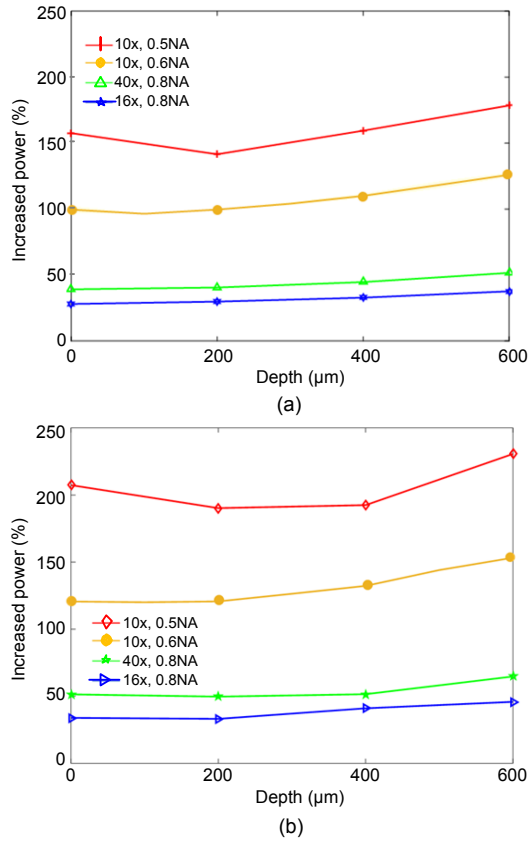

Fig. 5 Performance enhancements with different objectives in the human skin model

Increased collection with different objectives for fluorescent sources in the center (a) and at the edge (b) of the FOV

Contributors

Lingjie KONG proposed the main idea and guided the research. Ruheng SHI performed the simulations and drafted the manuscript. Cheng JIN and Chi LIU provided helpful suggestions on the result discussions and the manuscript organization. Ruheng SHI and Lingjie KONG revised and finalized the paper.

Compliance with ethics guidelines

Ruheng SHI, Cheng JIN, Chi LIU, and Lingjie KONG declare that they have no conflict of interest.

References

Allen CH, Hansson B, Raiche-Tanner O, et al., 2020. Coherent anti-Stokes Raman scattering imaging using silicon photomultipliers. *Opt Lett*, 45(8):2299-2302. https://doi.org/10.1364/OL.390050

Binding J, Arous JB, Léger JF, et al., 2011. Brain refractive index measured *in vivo* with high-NA defocus-corrected full-field OCT and consequences for two-photon microscopy. *Opt Expr*, 19(6):4833-4847. https://doi.org/10.1364/OE.19.004833

Chen JL, Voigt FF, Javadzadeh M, et al., 2016. Long-range population dynamics of anatomically defined neocortical networks. *eLife*, 5:e14679. https://doi.org/10.7554/eLife.14679.001

Cheong WF, Prahl SA, Welch AJ, 1990. A review of the optical properties of biological tissues. *IEEE J Quant Electron*, 26(12):2166-2185. https://doi.org/10.1109/3.64354

Combs CA, Smirnov AV, Riley JD, et al., 2007. Optimization of multiphoton excitation microscopy by total emission detection using a parabolic light reflector. *J Microsc*, 228(3):330-337. https://doi.org/10.1111/j.1365-2818.2007.01851.x

Denk W, Strickler JH, Webb WW, 1990. Two-photon laser scanning fluorescence microscopy. *Science*, 248(4951):73-76. https://doi.org/10.1126/science.2321027

Dvornikov A, Gratton E, 2016. Imaging in turbid media: a transmission detector gives 2-3 order of magnitude enhanced sensitivity compared to epi-detection schemes. *Biomed Opt Expr*, 7(9):3747-3755. https://doi.org/10.1364/BOE.7.003747

Engelbrecht CJ, Göbel W, Helmchen F, 2009. Enhanced fluorescence signal in nonlinear microscopy through supplementary fiber-optic light collection. *Opt Expr*, 17(8):6421-6435. https://doi.org/10.1364/OE.17.006421

Holtmaat A, Bonhoeffer T, Chow DK, et al., 2009. Long-term, high-resolution imaging in the mouse neocortex through a chronic cranial window. *Nat Protoc*, 4(8):1128-1144. https://doi.org/10.1038/nprot.2009.89

Jacques SL, 2013. Optical properties of biological tissues: a review. *Phys Med Biol*, 58(11):R37-R61. https://doi.org/10.1088/0031-9155/58/11/R37

Ji MB, Orringer DA, Freudiger CW, et al., 2013. Rapid, label-free detection of brain tumors with stimulated Raman scattering microscopy. *Sci Trans Med*, 5(201):201ra119. https://doi.org/10.1126/scitranslmed.3005954

Jin C, Kong LJ, Dana H, et al., 2020. Advances in point spread function engineering for functional imaging of neural circuits *in vivo*. *J Phys D Appl Phys*, 53(38):383001. https://doi.org/10.1088/1361-6463/ab946e

Kong LJ, Cui M, 2014. *In vivo* fluorescence microscopy via iterative multi-photon adaptive compensation technique. *Opt Expr*, 22(20):23786-23794. https://doi.org/10.1364/OE.22.023786

Kong LJ, Cui M, 2015a. *In vivo* deep tissue imaging via iterative multiphoton adaptive compensation technique. *IEEE J Sel Top Quant Electron*, 22(4):40-49. https://doi.org/10.1109/JSTQE.2015.2509947

Kong LJ, Cui M, 2015b. *In vivo* neuroimaging through the highly scattering tissue via iterative multi-photon adaptive compensation technique. *Opt Expr*, 23(5):6145-6150. https://doi.org/10.1364/OE.23.006145

Lichtman JW, Conchello JA, 2005. Fluorescence microscopy. *Nat Methods*, 2(12):910-919. https://doi.org/10.1038/nmeth817

Lister T, Wright PA, Chappell PH, 2012. Optical properties of human skin. *J Biomed Opt*, 17(9):090901. https://doi.org/10.1117/1.JBO.17.9.090901

Modi MN, Daie K, Turner GC, et al., 2019. Two-photon imaging with silicon photomultipliers. *Opt Expr*, 27(24): 35830-35841. https://doi.org/10.1364/OE.27.035830

Oheim M, Beaurepaire E, Chaigneau E, et al., 2001. Two-photon microscopy in brain tissue: parameters influencing the imaging depth. *J Neurosci Methods*, 111(1):29-37. https://doi.org/10.1016/S0165-0270(01)00438-1

Saar BG, Freudiger CW, Reichman J, et al., 2010. Video-rate molecular imaging in vivo with stimulated Raman scattering. *Science*, 330(6009):1368-1370. https://doi.org/10.1126/science.1197236

Soleimanzad H, Gurden H, Pain F, 2017. Optical properties of mice skull bone in the 455- to 705-nm range. *J Biomed Opt*, 22(1):010503. https://doi.org/10.1117/1.JBO.22.1.010503

Toublanc D, 1996. Henyey-Greenstein and Mie phase functions in Monte Carlo radiative transfer computations. *Appl Opt*, 35(18):3270-3274. https://doi.org/10.1364/AO.35.003270

Wang MR, Kim M, Xia F, et al., 2019. Impact of the emission wavelengths on *in vivo* multiphoton imaging of mouse brains. *Biomed Opt Expr*, 10(4):1905-1918. https://doi.org/10.1364/BOE.10.001905

Wang TY, Ouzounov DG, Wu CY, et al., 2018. Three-photon imaging of mouse brain structure and function through the intact skull. *Nat Methods*, 15(10):789-792. https://doi.org/10.1038/s41592-018-0115-y

Yang G, Pan F, Parkhurst CN, et al., 2010. Thinned-skull cranial window technique for long-term imaging of the cortex in live mice. *Nat Protoc*, 5(2):201-208. https://doi.org/10.1038/nprot.2009.222

Ruheng SHI, first author of this invited paper, received his BS degree in optoelectronic information science and engineering from Sichuan University, China, in 2018. He is now a PhD candidate at the Department of Precision Instrument, Tsinghua University, Beijing, China. His research focuses on optical imaging.

Lingjie KONG, corresponding author of this invited paper, received his BS degree from the Department of Optical Communication, Jilin University, China, in 2007, and his PhD degree from the Department of Precision Instrument, Tsinghua University, China, in 2012. He is now an associate professor at the Department of Precision Instrument, Tsinghua University, and a PI at the IDG/McGovern Institute for Brain Research, Tsinghua University. His research focuses on the interdisciplinary study of optoelectronics and biomedicine, aiming to motivate biomedical study by developing novel optical techniques.